

Constraining Black Hole Parameters in Non-Commutative Geometry using Machine Learning

Maryem Jemri*

ESMaR, Faculty of Science, Mohammed V University in Rabat, Rabat, Morocco

May 25, 2026

Abstract

Motivated by string theory, we constrain non-commutative black hole parameters through shadow behaviors using machine learning techniques combined by CUDA computations. To do so, we first investigate the structure of the event horizon of non-commutative black holes in the presence of string clouds and dark energy sectors by exploiting CUDA-based methods. We numerically approach the shadow properties and the energy emission rate of rotating and charged black holes in non-commutative geometry via such high-performance parallel computings. To bridge these findings with observational data, we implement a CUDA-based framework in order to constrain the involved black hole parameters including the non-commutative one. Using the resulting numerical data, we build a robust training datasets for a fully connected neural network to determine whether a given set of parameters matches with the observational data provided by Event Horizon Telescope collaborations. As a result, we find that the non-commutative model under study is consistent with the observations of $SgrA^*_{Kerr}$ black holes.

Keywords: Rotating and charged black holes in non-commutative geometry, EHT collaboration, CUDA numerical codes, Machine learning, fully connected neural network.

*maryem.jemri@um5r.ac.ma.

Contents

1	Introduction	3
2	NC quintessential rotating and black holes with a cloud of strings	5
3	NC black hole shadows and energy emission rate using CUDA computations	9
4	Constraints on NC rotating black hole parameters from EHT observations using CUDA techniques	15
5	Machine learning constraints on NC black hole parameters from EHT observations	17
5.1	Data preparation	18
5.2	FCNN classification of NC black hole shadow consistency with EHT observations	20
6	Concluding remarks	22

1 Introduction

Black hole thermodynamics including entropy, temperature, phase transitions, and critical phenomena has received particular importance [1–3]. These studies provide deep connections between several topics such as gravity, quantum mechanics, and statistical physics. Such connections have played a leading role in the current effort to develop a unified description of fundamental interactions.

Beyond standard general relativity, black hole solutions have been generalized within the framework of extended theories of gravity and modified geometric structures [4, 5]. In these approaches, the spacetime exhibits additional properties going beyond the classical Riemannian description. For instance, such deformations result from non-commutative (NC) geometry, modified derived structures, and gauge-theory descriptions of gravity, providing new classes of black hole solutions. It has been shown that the associated activities have refined certain classical results [6]. In particular, the implementation of NC geometry in the spacetime naturally induces modifications to the Einstein’s field equations [7–9]. In addition, extensions such as nonlinear Einstein electrodynamics modify the coupling between geometry and matter fields, giving rise to regular or deformed black hole configurations [10]. More generally, several effective gravitational theories can also incorporate contributions from dark matter or dark sector effects, which can modify the geometry and the dynamics of black holes [11]. In fact, these approaches provide a framework for understanding how spacetime geometric deformations and additional physical contributions can alert the black hole physical behaviors.

These theoretical developments have crucial consequences for observable signatures of black holes. Recently, considerable attention has been devoted to the optical properties of both rotating and non-rotating black holes in deformed spacetimes derived from various extensions of general relativity [12–20]. Many models have been investigated including black hole in Type II superstrings and M-theory where brane objects have been exploited in the examination of the associated physical behaviors [21–24]. It has been revealed that certain geometric corrections can modify photon trajectories, gravitational lensing effects, and shadow-related observables. Such effects are particularly relevant in empirical activities reported by the Event Horizon Telescope (EHT) collaboration, which provided the first direct images of supermassive black hole shadows [25–27]. To match theoretical predictions with observational data, high-performance numerical methods have been needed [28, 29]. In this context, CUDA has become a powerful platform for parallel computing based on NVIDIA GPUs [30, 31]. It has been shown that such numerical computations enable fast and scalable simulations, significantly reducing computation time while improving numerical accuracy. In black hole physics, these advantages are particularly important for shadow calculations and large parameter spaces investigations [32, 33]. Therefore, CUDA-based methods provide an efficient framework for confronting theoretical models with the observational results of the EHT collaboration.

In addition to numerical approaches, certain data-driven techniques have recently intro-

duced as powerful tools in black hole physics. Precisely, machine learning methods provide new ways to extract physical parameters, classify black hole configurations, and improve the reconstruction of observational images. Neural networks, for instance, can estimate accretion parameters from event-horizon-scale images [34]. Moreover, they could improve the quality of black-hole images obtained by the EHT international collaboration [35]. They have also been successfully applied to classify black holes in the mass–spin parameter space [36]. Furthermore, deep learning techniques have been extended to the analysis of gravitational-wave data, including the estimation of parameters for supermassive binary black holes in simulated LISA observations. These developments supply the growing role of machine learning as a complementary tool for probing the fundamental properties of black holes and analyzing increasingly complex astrophysical data.

The aim of this work is to contribute to such activities by constraining rotating and charged black hole parameters in NC geometry via shadow properties using machine learning techniques combined with CUDA methods. Before matching the obtained current theoretical predictions with the shadow observations reported by the EHT collaboration, we first discuss the horizon structure of NC black holes with string clouds in the presence of dark energy sector by providing numerical values using CUDA-based methods. Then, we investigate the shadows and the energy emission rate of NC rotating and charged black holes with the help of high-performance parallel computations. To bridge such findings with observational data, we develop a CUDA-based framework to establish relevant constraints on the NC parameter b , the cloud of strings parameter α , and the quintessence parameter N . Finally, we use these numerical results to construct reliable training data for a fully connected neural network (FCNN), in order to determine whether a given combination of parameters is consistent with EHT observational constraints. Precisely, we show that the trained FCNN accurately identifies the parameter space regions corresponding to the $M87^*$, $SgrA^*_{\text{VLTI}}$, and $SgrA^*_{\text{Keck}}$ black holes, with predictions evaluated within the $1 - \sigma$ and $2 - \sigma$ confidence intervals from the EHT collaboration. As a result, we find that the proposed model matches with the $SgrA^*_{\text{Keck}}$ observational findings.

The organization of the paper is as follows. In section 2, we reconsider the study of rotating and charged black holes with a cloud of strings and quintessence fields in NC geometry. Section 3 is devoted to the investigation of the shadows and the energy emission rate of such NC rotating and charged black holes using CUDA techniques. Section 4 bridges the theoretical predictions with observational data from the EHT collaboration through CUDA-based computations. In section 5, we exploit machine learning methods to classify whether the reduced parameter space of such NC black holes is consistent with the observations of $M87^*$, $SgrA^*_{\text{VLTI}}$, and $SgrA^*_{\text{Keck}}$. Finally, the last section exposes some concluding remarks.

2 NC quintessential rotating and black holes with a cloud of strings

In this section, we reconsider the study of rotating and charged black holes in NC spacetime, characterized by a single parameter Θ . Such NC structures have attracted considerable attention in recent years, particularly in the investigation of black hole physical behaviors [37]. These studies have been supported by supergravity models where the NC geometry naturally arises in string theory with D-brane configurations in the presence of a Neveu–Schwarz antisymmetric B -field [38]. NC spaces have been approached using physical and geometrical contributions. In particular, the gauge theories on such spaces have been investigated [39]. Moreover, it has been suggested that NC parameters can be exploited to remove certain singularities of complex geometries including Calabi-Yau varieties with ADE configurations [40–43]. Setting $\hbar = 1$, the spacetime coordinates are interpreted as non-commuting operators satisfying the commutations relations

$$[x^\mu, x^\nu] = i\theta^{\mu\nu}, \quad (2.1)$$

where $\theta^{\mu\nu}$ is a constant antisymmetric tensor. In the strong-field limit, it has been shown that this tensor is related to the inverse of the stringy field B considered as a fundamental object in string theory. For simplicity reasons, we consider the reduced form

$$\theta^{\mu\nu} = \Theta \epsilon^{\mu\nu}, \quad (2.2)$$

where $\epsilon^{\mu\nu}$ is the antisymmetric Levi-Civita tensor and Θ is a NC parameter with dimensions of length squared. This provides an economical model involving only one parameter. The present framework could be considered as an effective phenomenological description of NC gravitational effects rather than a complete quantum gravity theory [49]. In this way, the non-commutativity parameter Θ can be assumed to provide leading NC corrections to the black hole geometry [37]. The generated solutions are mainly valid in the regime where the NC scale $\sqrt{\Theta}$ remains small compared to the size of the black hole. Precisely, here, we investigate rotating and charged black hole solutions in such NC backgrounds by analyzing the impact of Θ on their geometric and physical properties including the optical ones. This framework could provide a phenomenological setting that sheds light on the physics of black holes in non-trivial theories of gravity, notably on D-brane configurations and type II string backgrounds. It has been assumed that the dynamics of such systems could be described by the Einstein–Hilbert action which can be expressed as follows

$$S = \int d^4x \frac{\sqrt{-g}}{16\pi G} [\mathcal{R} + \mathcal{L}_m + \mathcal{L}_c], \quad (2.3)$$

where \mathcal{L}_m and \mathcal{L}_c represent the matter and the charge contributions, respectively [44]. To approach the associated behaviors, one could consider a static and spherically symmetric spacetime which reads as

$$ds^2 = -f(r)dt^2 + \frac{dr^2}{f(r)} + r^2 d\theta^2 + r^2 \sin^2 \theta d\phi^2, \quad (2.4)$$

where the metric function takes the following form

$$f(r) = 1 - \frac{2m(r)}{r} + \frac{q^2(r)}{r^2}. \quad (2.5)$$

The radial functions $m(r)$ and $q(r)$ can be determined by solving the Einstein equations of motion which can be expressed as follows

$$G_{\mu\nu} + \Lambda g_{\mu\nu} = 8\pi T_{\mu\nu}, \quad (2.6)$$

where the stress energy tensor can be split as

$$T_{\mu\nu} = T_{\mu\nu}^m + T_{\mu\nu}^c \quad (2.7)$$

according to the mass and the charge contributions, respectively. In NC geometry, such distributions are modeled by Lorentzian profiles

$$\rho_M(r) = \frac{M\sqrt{\Theta}}{\pi^{3/2}(r^2 + \Theta)^2}, \quad \rho_Q(r) = \frac{Q\sqrt{\Theta}}{\pi^{3/2}(r^2 + \Theta)^2}, \quad (2.8)$$

where Θ denotes the NC parameter with dimension $[L^2]$ [45, 46]. In this way, Q represents the black hole charge, while M denotes the total mass distributed over a region with a linear size of order $\sqrt{\Theta}$ [47, 48]. The smeared mass and the charge distribution functions can be expressed as

$$\begin{aligned} m(r) &= \int_0^r \rho_M(r) 4\pi r^2 dr, \\ q(r) &= \int_0^r \rho_Q(r) 4\pi r^2 dr. \end{aligned} \quad (2.9)$$

Roughly, the calculations gives the following expressions

$$\begin{aligned} m(r) &= \frac{2M}{\pi} \arctan\left(\frac{r}{\sqrt{\pi\Theta}}\right) - \frac{2M\sqrt{\Theta}}{\sqrt{\pi}} \frac{r}{r^2 + \pi\Theta}, \\ q(r) &= \frac{2Q}{\pi} \arctan\left(\frac{r}{\sqrt{\pi\Theta}}\right) - \frac{2Q\sqrt{\Theta}}{\sqrt{\pi}} \frac{r}{r^2 + \pi\Theta}. \end{aligned} \quad (2.10)$$

Considering the regime $r \gg \sqrt{\Theta}$, these expressions reduce to

$$m(r) = M - \frac{4M\sqrt{\Theta}}{\sqrt{\pi}r} + \mathcal{O}\left(\frac{\Theta^{3/2}}{r^3}\right), \quad (2.11)$$

$$q(r) = Q - \frac{4Q\sqrt{\Theta}}{\sqrt{\pi}r} + \mathcal{O}\left(\frac{\Theta^{3/2}}{r^3}\right). \quad (2.12)$$

It is worth nothing that the above expansion indicates that the resulting metric can be viewed as an approximate version in the weak NC regime [49]. Substituting these expressions into the metric function, one gets the following non-rotating solutions in NC geometry

$$f(r) = 1 - \frac{2M}{r} + \frac{8M\sqrt{\Theta}}{\sqrt{\pi}r^2} + \frac{Q^2}{r^2} - \frac{8Q^2\sqrt{\Theta}}{\sqrt{\pi}r^3} + \mathcal{O}(\Theta^{3/2}). \quad (2.13)$$

In addition to the internal black hole parameters M , and Q , a set of effective deformation parameters could be implemented in order to enlarge the associated moduli space. Moreover, one accounts for rotations by introducing the spin parameter a which leads to the following spacetime metric

$$ds^2 = \frac{\sigma(r)}{\Sigma(r)} dt^2 - \frac{2a\sigma(r)\sin^2\theta}{\Sigma(r)} dt d\phi + \frac{\Sigma(r)}{\Delta(r)} dr^2 + \Sigma(r) d\theta^2 + \frac{r^2 + a^2 + a^2\sigma(r)\sin^2\theta}{\Sigma(r)} \sin^2\theta d\phi^2, \quad (2.14)$$

where the metric functions are defined by

$$\Sigma(r) = r^2 + a^2 \cos^2 \theta, \quad \Delta(r) = r^2 f(r) + a^2, \quad \sigma(r) = r^2(1 - f(r)). \quad (2.15)$$

Motivated by several previous works, including the recent studies reported in [50], the effective metric function incorporates extra contributions going beyond the ordinary black hole configurations. In this present work, we further extend the NC model by including additional external effects in order to describe more realistic astrophysical and cosmological environments. Precisely, we focus mainly on the impact of the non-commutativity aspect as well as surrounding matter fields which could influence the black hole geometry and its observable properties. These extensions could be motivated by the fact that realistic black holes are generally not isolated systems. However, they are expected to be embedded in non-trivial backgrounds involving both quantum-inspired corrections and large-scale matter distributions. For such reasons, we consider the following extended form

$$f(r) = 1 - \alpha - \frac{2M}{r} + \frac{bM}{r^2} + \frac{Q^2}{r^2} - \frac{bQ^2}{r^3} - \frac{N}{r^{3w+1}} \quad (2.16)$$

where one has introduced a new non-commutativity parameter form which reads as

$$b = \frac{8\sqrt{\Theta}}{\sqrt{\pi}}. \quad (2.17)$$

The terms bM/r^2 and $-bQ^2/r^3$ arise as perturbative NC corrections in the large-radius regime, consistent with the Gaussian-smearred source models [51, 52]. Other external parameters have been included such as the string cloud parameter α and the quintessence ones. In particular, N and w represent the dark section field contributions [53]. A close inspection demonstrates that the metric functions generate a black hole moduli space \mathcal{M}_{bh} which can be split as

$$\mathcal{M}_{bh} = \mathcal{M}_{int} \times \mathcal{M}_{ext} \quad (2.18)$$

where the first factor controls the internal parameters

$$\mathcal{M}_{int} = \{M, Q, a\} \quad (2.19)$$

while the second one represents the external ones

$$\mathcal{M}_{ext} = \{b, \alpha, N, w\}. \quad (2.20)$$

A careful examination reveals that one can consider certain special regions by fixing the value of w . For simplicity reasons, we set $w = -\frac{2}{3}$. After fixing certain regions in the black hole moduli space, we examine the existence of horizons using a numerical approach implemented in CUDA, which enables efficient parallel computations on GPU architectures. It is denoted that CUDA is a general-purpose computing platform and programming models exploiting the parallel computing capabilities of NVIDIA GPUs. In this method, the GPU's architecture enables the distribution of computational tasks across a large number of streaming multiprocessors (SMs), which ensures a highly efficient parallel processing. Moreover, the modern GPU's provide advanced optimization techniques and tools enhancing the computational performance. With each new generation, improvements in the CUDA core architecture lead to increased efficiency and reduced computation time. In this context, the CUDA has proven to be a powerful tool in the black hole physics, enabling efficient GPU-accelerated simulations [54–56]. This significantly not only reduces computational cost but also improves the numerical efficiency. Besides, it can facilitate the exploration of theoretical predictions in strong gravity regimes [57, 58]. To verify the numerical reliability of the present analysis, additional tests have been performed by changing the integration step and the grid resolution used in the simulations. The obtained results show stable convergence with only small numerical deviations, indicating a satisfactory numerical precision in the explored parameter space [59–61]. In fact, the CUDA-based GPU implementation considerably reduces the computation time compared to standard CPU calculations, especially for large parameter scans and high-resolution numerical simulations [62, 63]. This acceleration makes the present framework suitable for extensive computations involving many parameter configurations and geodesic evaluations [64, 65]. Roughly, the horizons are identified by vanishing the inverse of the radial component of the metric function. To probe their existence, we employ a numerical method in which the parameters Q , α , and N remain constant, while the parameter b varies from 0 to 0.3 in increments of 0.1. The parameter a can be adjusted over the same range using the same step size. For each pair (a, b) , the horizon equation is solved numerically in order determine whether there exists at least one real root corresponding to a physically meaningful horizon in black hole physics. This systematic procedure provides a way to identify the regions of the reduced back hole moduli space in which these solutions are acceptable. Fig. (1) illustrates such behaviors by displaying the regions in the (a, b) plane where at least one real horizon exists, for different values of N and α .

This figure shows that increasing the parameter α reduces the regions of the parameter space which supports the existence of physical horizons. Based on these results, the forthcoming optical analysis will be conducted within the parameter subsets which correspond to configurations admitting at least one real horizon in the associated black hole physics.

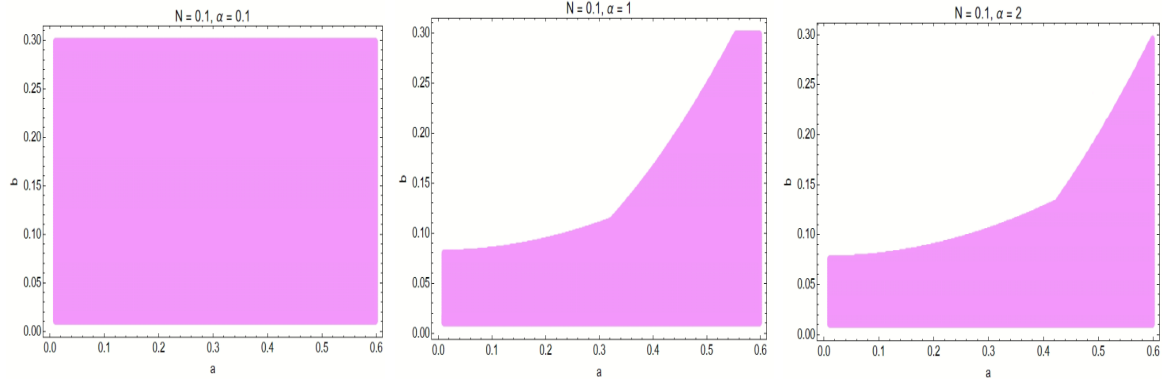


Figure 1: Regions in the (a, b) plane where the metric admits at least one real event horizon radius.

3 NC black hole shadows and energy emission rate using CUDA computations

In this section, we investigate certain optical properties of rotating and charged NC black holes with a cloud of strings and quintessence in NC geometry by applying CUDA techniques. Precisely, we analyze the effect the involved parameters on both the black hole shadow and the energy emission rate. To elaborate this analysis, we employ a CUDA-based numerical code enabling high-performance parallel computations. It is denoted that the shadow of a black hole is defined as the apparent dark region bounded by the critical curve observed when light rays approach unstable circular photon orbits before being captured or scattered [66–69]. This optical aspect can be examined by approaching the null geodesics in the black hole spacetime. On the other hand, the energy emission rate is directly linked to the absorption cross section of the black hole which provides significant information about its thermodynamic and radiative properties. To investigate the optical properties of such rotating and charged NC black holes, roughly, we establish the associated equations of motion by implementing the CUDA techniques in the Hamilton–Jacobi formalism via the separation of variables according to the Carter method [70]. For the above NC black hole solutions, the resulting equations of motion can be expressed as follows

$$\Sigma \dot{t} = \frac{r^2 + a^2}{\Delta} [E (r^2 + a^2) - aL] + a [L - aE \sin^2 \theta] \quad (3.1)$$

$$(\Sigma \dot{r})^2 = \mathcal{R}(r) \quad (3.2)$$

$$(\Sigma \dot{\theta})^2 = \Theta(\theta) \quad (3.3)$$

$$\Sigma \dot{\phi} = [L \csc^2 \theta - aE] + \frac{a}{\Delta} [E (r^2 + a^2) - aL], \quad (3.4)$$

where E and L are the energy and the angular momentum of the light rays, respectively. $\mathcal{R}(r)$ and $\Theta(\theta)$ are radial functions which read as

$$\mathcal{R}(r) = [E(r^2 + a^2) - aL]^2 - \Delta [\mathcal{C} + (L - aE)^2], \quad (3.5)$$

$$\Theta(\theta) = \mathcal{C} - (L \csc \theta - aE \sin \theta)^2 + (L - aE)^2, \quad (3.6)$$

where \mathcal{C} is a Carter separation parameter. Solving the unstable circular orbit equations, one needs two impact parameters being given by

$$\xi = \frac{r^2 [16a^2 \Delta(r) + 8r \Delta(r) \Delta'(r)^2 - r^2 \Delta'(r)^2]}{a^2 \Delta'(r)^2} \Big|_{r=r_0}, \quad (3.7)$$

$$\Xi = \frac{(r^2 + a^2) \Delta'(r) - 4r \Delta(r)}{a \Delta'(r)} \Big|_{r=r_0}. \quad (3.8)$$

In the case of rotating black holes with a cloud of strings and quintessence fields in NC geometry, the apparent shadow, at spatial infinity, can be illustrated using the celestial coordinates (X, Y) which are expressed as follows

$$X = \lim_{r_{\text{ob}} \rightarrow +\infty} \left(-r_{\text{ob}}^2 \sin \theta_{\text{ob}} \frac{d\phi}{dr} \right)$$

$$Y = \lim_{r_{\text{ob}} \rightarrow +\infty} \left(r_{\text{ob}}^2 \frac{d\theta}{dr} \right),$$

where r_{ob} denotes the distance between the observer and the black hole. The quantity θ_{ob} represents the inclination angle between the observer line of the sight and the rotation axis of the black hole. To investigate the influence of each parameter on the black hole shadows, we employ a numerical approach to provide the corresponding graphical representation for acceptable ranges of the involved black hole parameters. More specifically, a CUDA-based parallel computing program has been used to accelerate the calculations [71,72], which allows for the efficient determination of the shadow boundaries for different parameter variations. For each set of shadow curves, all parameters are held constant except for the parameter of interest, which is varied in increments of 0.01. Considering the special case $w = -\frac{2}{3}$, we solve Eqs. (3.7) and (3.8) and substitute the resulting expressions into the shadow equation. This procedure permits to accurately evaluate the influence of each parameter on the geometric deformation of the shadow, affecting both its size and shape. In Fig. (2), we illustrate the black hole shadows by analyzing the effects of the charge Q and the rotation parameter a , by taking $b = 0.1$ and $\alpha = 0.1$.

As shown in the figure, the rotation parameter a exhibits behaviors similar to that in standard black hole solutions. Indeed, it slightly reduces the size of the shadow and deforms the shape into a D-like structure. This confirms that a keeps its role as a deformation parameter in these configurations. Increasing Q , however, the size of the shadow decreases without affecting the shape, which is consistent with the behavior observed in ordinary charged black holes. However, in the present model, the range of variation in the shadow

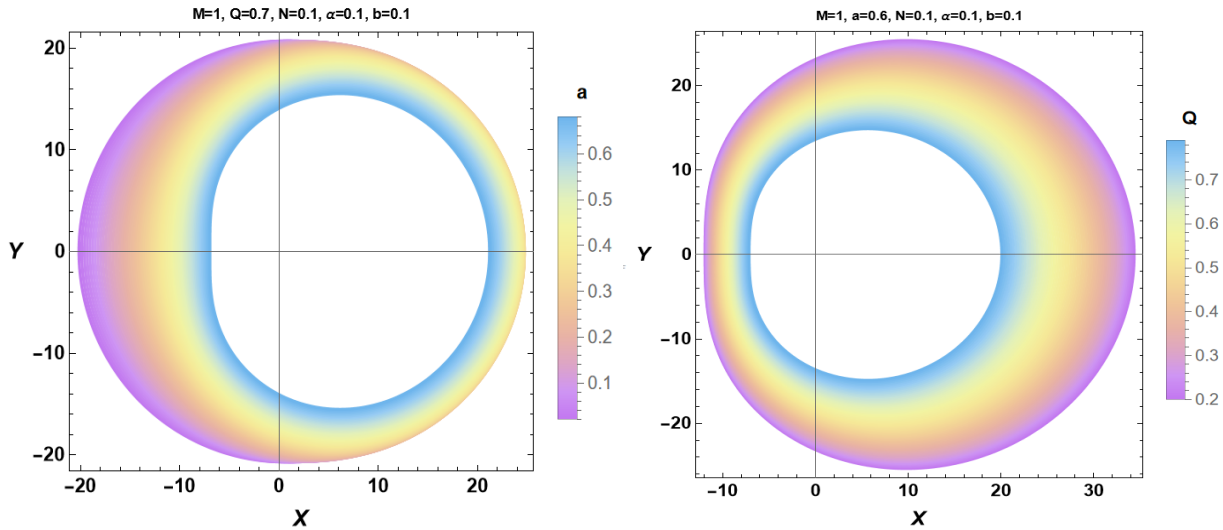


Figure 2: *Effect of internal parameters on the shadow behavior.*

size extends up to values of approximately 45, unlike ordinary charged black holes, where the radius generally does not exceed 25. This difference can be attributed to the additional terms in the metric, in which the parameter b couples with the charge Q . Then, the effect of the string cloud parameter α and the quintessence parameter N are examined by varying one while keeping the other one fixed, thereby isolating their respective contributions. For $b = 0.1$, the variation of α and N increases the overall size of the black hole shadow.

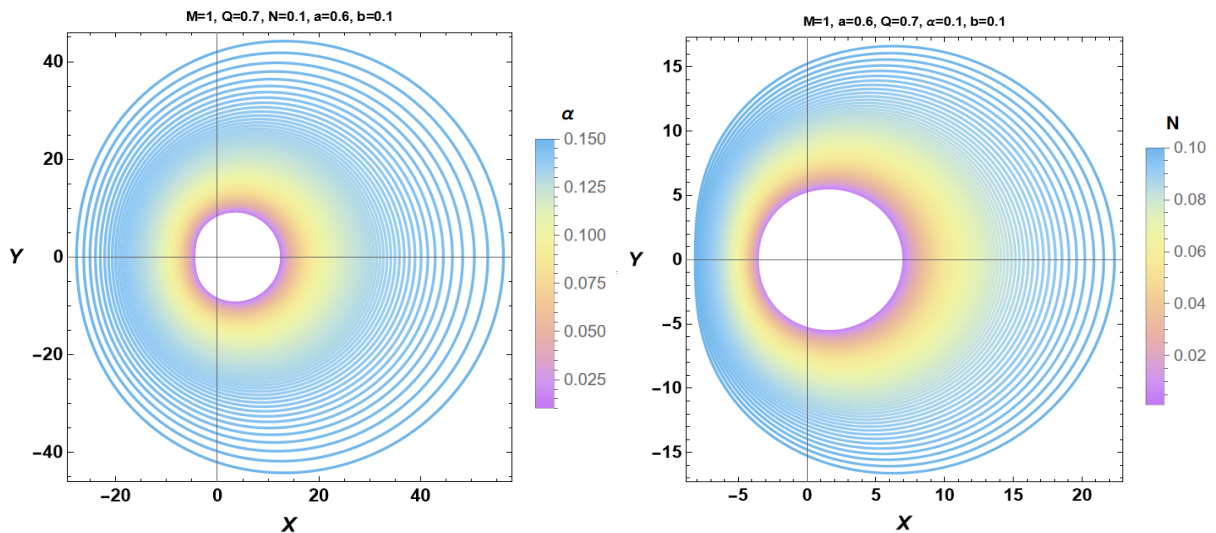


Figure 3: *Effect of α (left panel) and N (right panel) on the black hole shadow behavior.*

As illustrated in Fig. (3), the shadow exhibits a D-like deformation in the regime of large N and small α . This characteristic gradually reduces as α increases or N decreases, which indicates that these two parameters have a similar influence on the distortion of the shadow curves.

We now examine the effect of the NC parameter b on the shadow behaviors. As shown

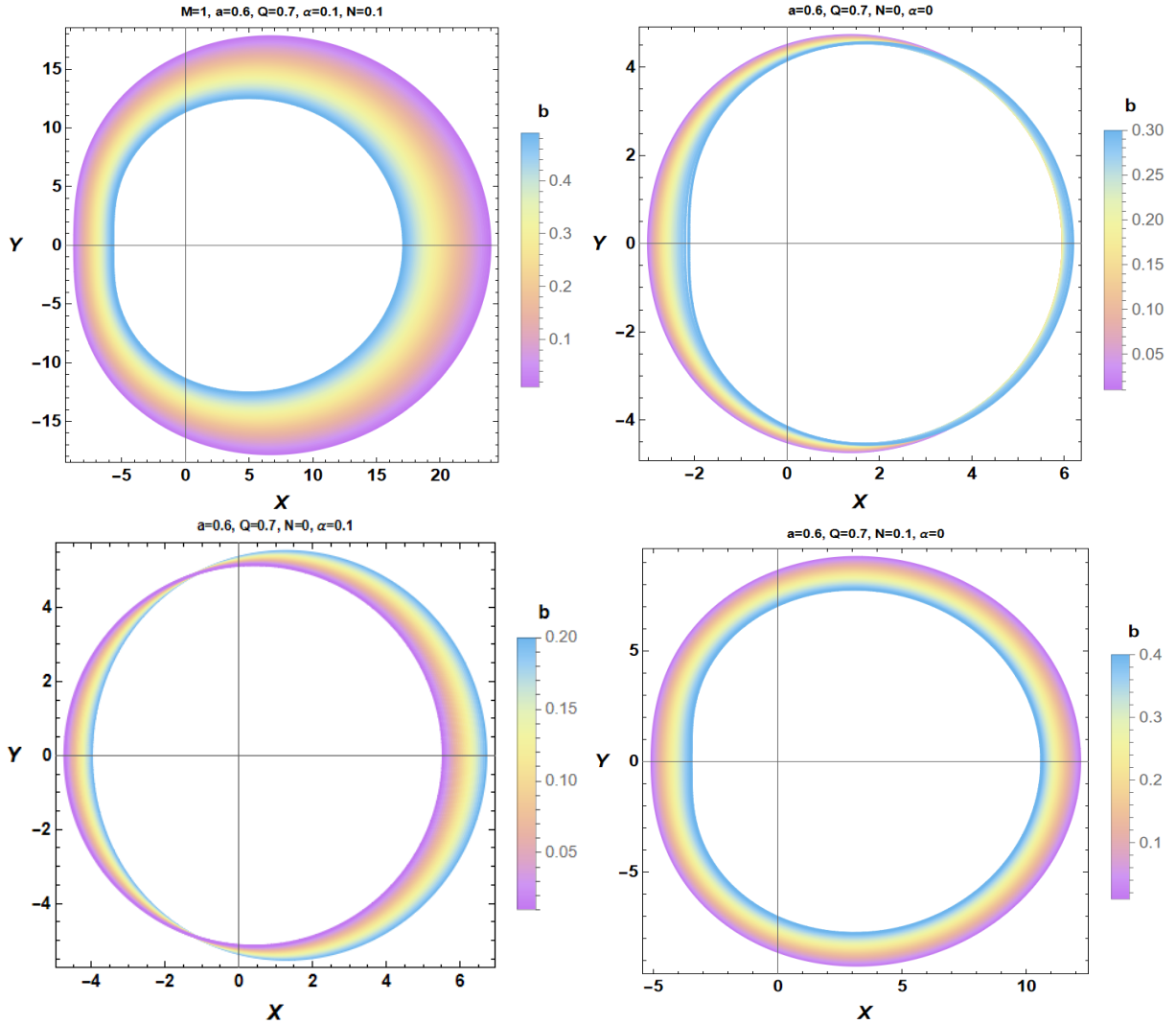


Figure 4: *Effect of the parameter b on the shadow behavior.*

in Fig. (4), such a parameter controls both the size and the global shape of the shadow. Increasing b leads to a larger and more extended shadows, whereas smaller values of b yield a more compact and nearly circular geometric configurations.

In contrast, the parameters N and α have less effects, mainly changing the shape of the shadow boundary rather than its size. Consequently, b sets the characteristic size of the shadow, while N and α control deviations from the circularity and the resulting distortions of its shape.

To go beyond the discussion of the shadow properties of black holes with a cloud of strings and the quintessence in NC geometry, we employ a CUDA-based numerical method to evaluate the energy emission rate associated with rotating black holes in this non-trivial framework. By leveraging the parallelism of GPUs, this approach provides efficient and high-performance computations of the effective absorption cross sections over a wide range of parameters. For a distant observer, the absorption cross section at very high energies asymptotically can reach a geometric optics limit, which is directly related to the size of the

black hole shadow. At intermediate energy regimes, the effective absorption cross section exhibits oscillations around a constant value, denoted by σ_{lim} . It has been shown that this limiting value coincides with the geometric cross section of the photon sphere, which is determined by the properties of null geodesics [73–75]. Since the shadow encodes the optical appearance of the black hole, it can be identified with this limiting cross section. Therefore, σ_{lim} can be approximated as follows

$$\sigma_{\text{lim}} \simeq \pi R_s^2, \quad (3.9)$$

where R_s represents the radius of the black hole shadow. In this context, the differential energy emission rate can be written as

$$\frac{d^2 E(\omega)}{d\omega dt} = \frac{2\pi^3 R_s^2}{e^{\omega/T_H} - 1} \omega^3, \quad (3.10)$$

where T_H denotes the Hawking temperature of the black hole and ω represents the emission frequency. This relation establishes a direct connection between the thermodynamic properties of the black hole and its optical features. In particular, it generates a useful framework for probing spacetime parameters through observational signatures. For the rotating metric solutions, the Hawking temperature of such black holes reads as

$$T_H = \frac{2r(1 - \alpha) - 2M + \frac{bQ^2}{r^2} - \frac{N(1-w)}{r^{2w}}}{4\pi(a^2 + r^2)}. \quad (3.11)$$

To evaluate the energy emission rate for different black hole parameter values, we perform numerical simulations using a CUDA-based program. The corresponding code first computes the maximal shadow radius from the obtained optical data. Then, the horizon radius is determined by solving $\Delta(r_h) = 0$. Moreover, the result is substituted into the Hawking temperature expression. Taking the specific case $w = -\frac{2}{3}$, we assess the influence of each parameter by varying the parameter of interest in steps of 0.01 while keeping all other parameters fixed. The resulting data are then used to generate the energy emission rate plots.

In Fig. (5), we present the variation of the energy emission rate as a function of the emission frequency. The figure consists of two panels. The first one illustrates the effect of the electric charge, while the second one shows the effect of the rotation parameter. This comparison unveils the role of such parameters in the emission process graphical representation.

It has been observed from both panels that increasing either the charge Q or the rotation parameter a leads to an initial enhancement of the energy emission rate up to a critical value, after which the emission rate decreases. Thus, both Q and a manifest a non-monotonic behavior, acting as amplifying factors at low values and as suppressing effects beyond their respective critical thresholds.

Fig. (6) shows the effects of the parameters α and N on the energy emission rate. Both α and N produce a clear suppression of the energy emission rate. This behavior indicates that increasing either α or N reduces the efficiency of the radiation process in this regime. Thus,

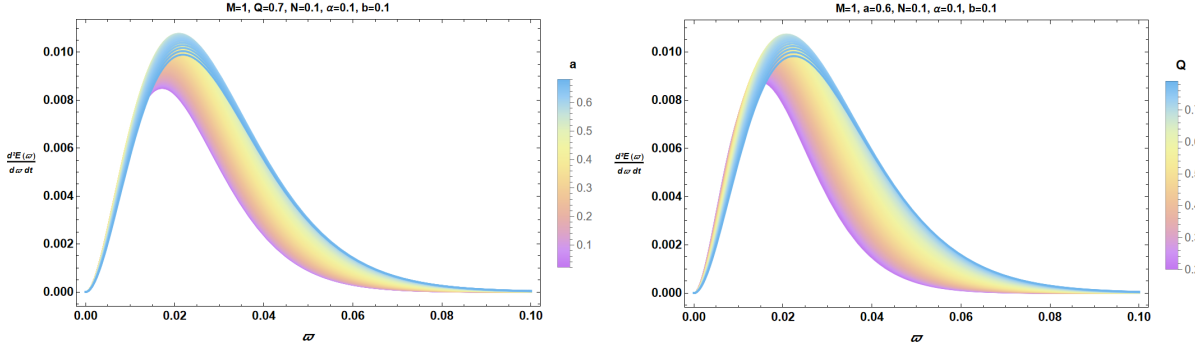


Figure 5: Variation of the energy emission rate as a function of the emission frequency for different values of a and Q .

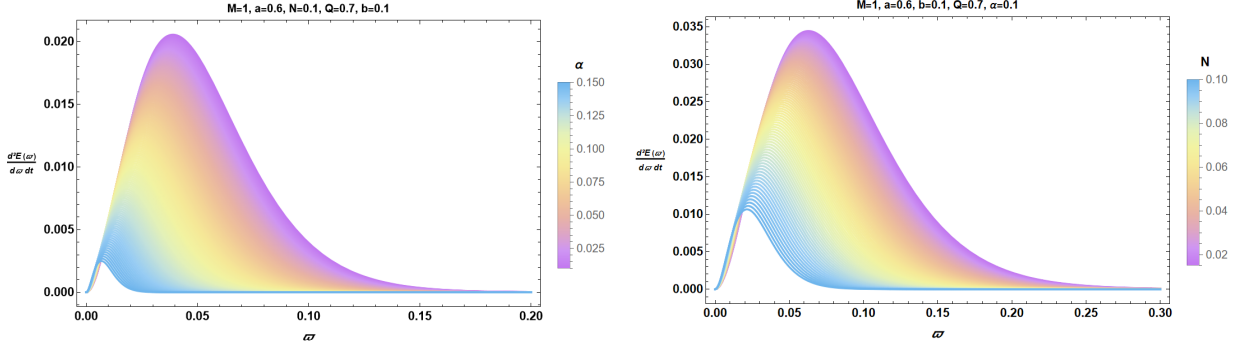


Figure 6: Variation of the energy emission rate as a function of the emission frequency for different values of η .

these results clearly show the attenuating effect of these two parameters on the emission spectrum.

From the four panels in Fig. (7), we analyze the effect of the NC parameter b on the energy emission rate for different values of N and α . In all cases, the general behavior follows a similar behavior. Indeed, the energy emission rate increases to a maximum value and then decreases as the frequency parameter increases. It is clear that an increase in b results in a reduction in the peak emission rate as well as a decrease in the overall amplitude of the curve. This means that higher values of b reduce the energy emission process and make the radiation less intense. This behavior is consistent in all subgraphs, independent of the values selected for N and α . Moreover, it indicates that b has a reducing effect on the emission spectrum.

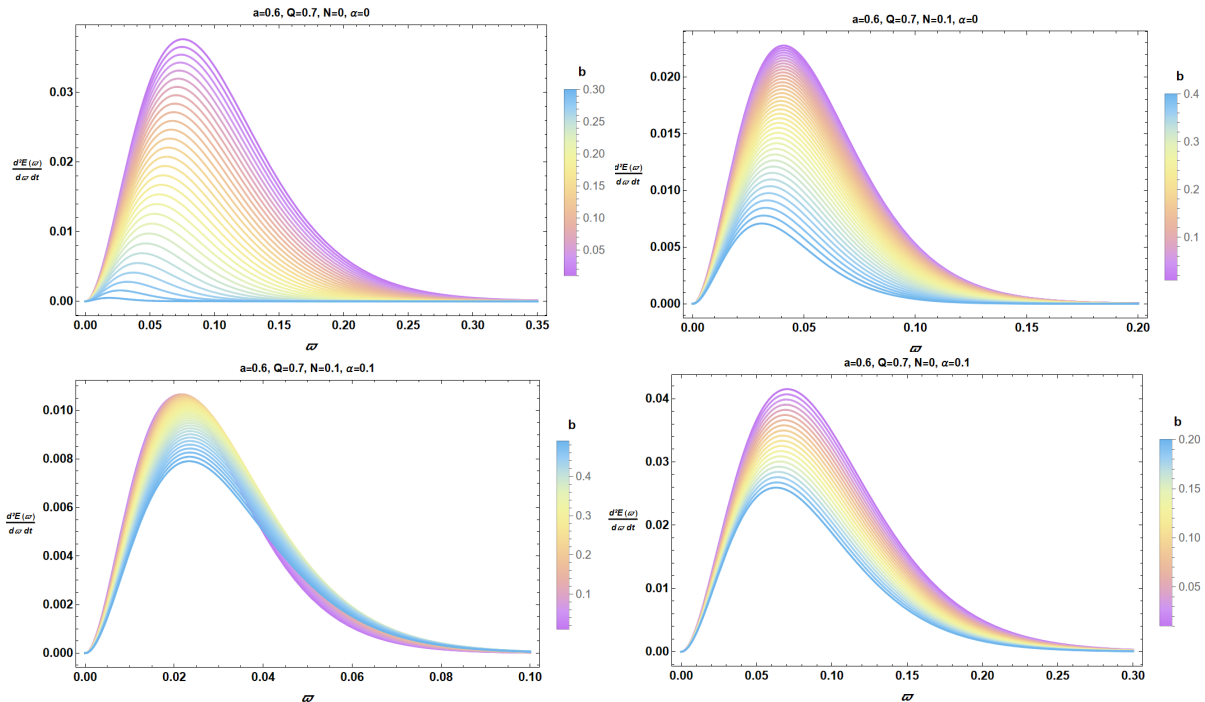


Figure 7: Variation of the energy emission rate as a function of the emission frequency for different values of b .

4 Constraints on NC rotating black hole parameters from EHT observations using CUDA techniques

In order to establish a bridge between the theoretical predictions and the observational data, this section provides an analysis of the shadow cast by rotating NC quintessence Reissner–Nordström black holes with a cloud of strings, in comparison with observational results reported by EHT empirical findings. Precisely, we use the observational data of the M87* and Sgr A* black holes to constrain the parameters of these black hole models [76–78]. In the present work, the numerical analysis has been carried out using a CUDA-based code developed by NVIDIA, which exploits GPU parallel computing to significantly accelerate the computations required for determining the black hole shadows. In practice, the constraints can be obtained by using the fractional deviation from the Schwarzschild black hole shadow diameter, defined as

$$d = \frac{R_s}{r_{sh}} - 1, \quad (4.1)$$

where R_s denotes the shadow radius and r_{sh} represents the Schwarzschild radius. The dimensionless ratio R_s/M serves as a primordial observable to confront the theoretical models with observational data. The 1σ and 2σ confidence intervals derived from the EHT observations are displayed in Table 1.

In the following discussion, we present a numerical procedure based on CUDA parallel computations to determine the parameter pairs (α, b) , (N, b) , (a, b) , and (Q, b) that yield

Black hole	Deviation (d)	1- σ bounds	2- σ bounds
M87* (EHT)	$-0.01^{+0.17}_{-0.17}$	$4.26 \leq \frac{R_s}{M} \leq 6.03$	$3.38 \leq \frac{R_s}{M} \leq 6.91$
Sgr A* (EHT _{VLT})	$-0.08^{+0.09}_{-0.09}$	$4.31 \leq \frac{R_s}{M} \leq 5.25$	$3.85 \leq \frac{R_s}{M} \leq 5.72$
Sgr A* (EHT _{Keck})	$-0.04^{+0.09}_{-0.10}$	$4.47 \leq \frac{R_s}{M} \leq 5.46$	$3.95 \leq \frac{R_s}{M} \leq 5.92$

Table 1: *Fractional deviations and corresponding bounds for M87* and Sgr A* black holes.*

black hole shadow configurations consistent with EHT observational data. In each case, all parameters are fixed except for b , which is the parameter we aim to constrain. The second parameter in each pair is varied within the allowed range of the model parameter space. For each choice of parameters, the maximal shadow radius R_{\max} has been computed using a CUDA-based code, enabling an efficient evaluation over a dense grid in the parameter space. The resulting shadow radius is then compared with the observational bounds provided by EHT collaboration. This comparison identifies the parameter space regions that meet with the $1 - \sigma$ and $2 - \sigma$ confidence interval conditions. The numerical computations are given in Fig. (8).

As illustrated in Fig. (8), the regions of the reduced parameter spaces (α, b) , (a, b) , (Q, b) , and (N, b) that are consistent with observational data tend to expand for larger values of the parameters. This behavior shows that the black hole spacetime can reproduce the shadow signatures observed in a relatively large range of configurations, demonstrating the flexibility of the model. Due to links between parameters, in each analysis one parameter is fixed while the other is varied within its allowed range. In all considered parameter subspaces (α, b) , (Q, b) , (a, b) , and (N, b) , the metric admits wide ranges of the parameter values being compatible with the existence of real and physically meaningful horizons. Confronted with observational data, however, these ranges become significantly constrained.

The corresponding constraints for M87* and Sgr A* at the $1 - \sigma$ and $2 - \sigma$ confidence levels are summarized in Table (2), together with the results being obtained for all parameter spaces. In this analysis, we fix $w = -2/3$ throughout, and adopt the reference values $(a = 0.5, Q = 0.5, N = 0.1, \alpha = 0.1)$. For each figure, only one parameter is varied within its allowed range, while the remaining parameters are kept fixed.

A clear conclusion emerges from this examination. Indeed, although the parameter space theoretically allows for large regions, only limited regions are compatible with the observational constraints. In particular, the NC parameter b plays a major role, as it is consistently constrained by the data in all cases, whereas the other parameters primarily influence the shape and the size of the allowed regions. This indicates that b behaves as a control parameter governing the agreement between the theoretical model and the observed black hole shadows.

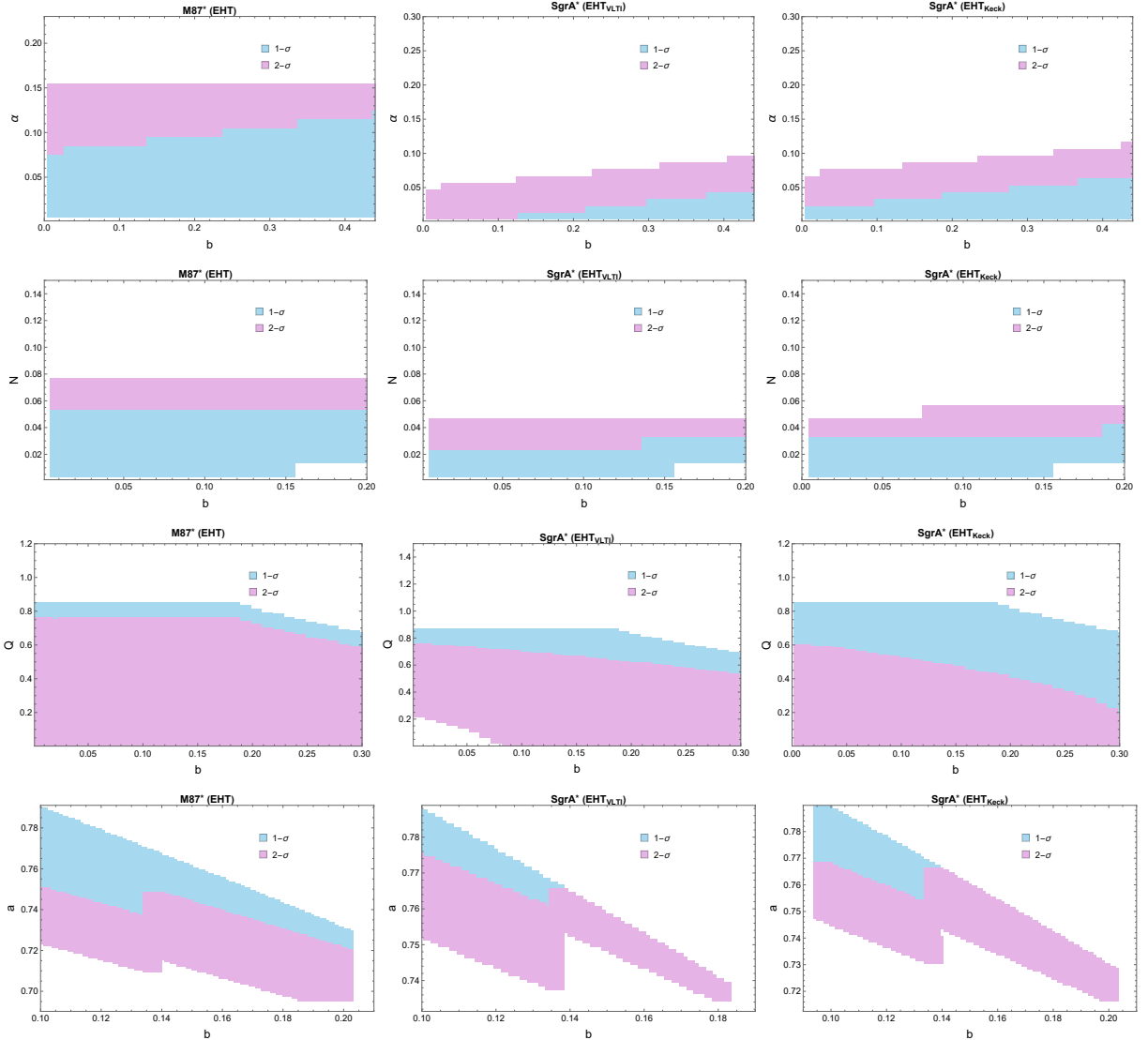


Figure 8: Combined constraint regions in the parameter spaces (α, b) , (Q, b) , (a, b) , and (N, b) obtained from CUDA-based simulations.

5 Machine learning constraints on NC black hole parameters from EHT observations

In this section, we would like to apply machine learning techniques to the shadow activities. This approach has been motivated by recent developments in the application of machine learning to the physics of black hole physics and superstring theory compactifications on Calabi–Yau manifolds. For instance, these methods have been exploited in the classical classification of black holes in the mass–spin diagram as well as in quantum gravitational settings [79, 80]. In the context of string theory compactifications, machine learning methods have been successfully employed to analyze and classify complex geometric data, including complete intersection Calabi–Yau manifolds and their free quotients using neural networks [81]. Moreover, certain studies demonstrate that machine learning models are ca-

Table 2: Constraints on the parameter b for different fixed values of α , a , N , and Q , derived from observational bounds at the $1 - \sigma$ and $2 - \sigma$ confidence levels.

Parameter	Confidence	$M87^*$	$Sgr A_{\text{VLTI}}^*$	$Sgr A_{\text{Keck}}^*$
$\alpha = 0.04$	$1 - \sigma$	$0.01 < b < 0.44$	$0.38 < b < 0.44$	$0.01 < b < 0.44$
	$2 - \sigma$	$0.01 < b < 0.44$	$0.01 < b < 0.44$	$0.10 < b < 0.44$
$N = 0.035$	$1 - \sigma$	$0.01 < b < 0.20$	$0.01 < b < 0.20$	$0.01 < b < 0.20$
	$2 - \sigma$	$0.01 < b < 0.20$	$0.14 < b < 0.20$	$0.19 < b < 0.20$
$Q = 0.7$	$1 - \sigma$	$0.01 < b < 0.28$	$0.01 < b < 0.30$	$0.01 < b < 0.25$
	$2 - \sigma$	$0.01 < b < 0.20$	$0.01 < b < 0.10$	$0.01 < b < 0.30$
$a = 0.76$	$1 - \sigma$	$0.01 < b < 0.145$	$0.13 < b < 0.136$	$0.11 < b < 0.132$
	$2 - \sigma$	$0.01 < b < 0.145$	$0.1 < b < 0.142$	$0.1 < b < 0.42$

pable of efficiently identifying physical regimes and structural properties of black holes based on their parameter space. In particular, neural networks can detect transition boundaries between different classes of black holes, predict regions of stability, and uncover hidden geometric structures. Supported by such developments, we employ machine learning techniques, specifically feed-forward FCNN [82], to generate black hole shadow configurations consistent with observational data from the EHT. A priori, there are many models to follow. However, here, we exploit a FCNN since it is a simple. Moreover, it is a fast model that can learn the relation between the physical parameters and the observational constraints [83, 84]. It has been well suited for problems with a small number of input parameters giving stable results with low computational costs. For such a reason, it is useful to probe large regions of the black hole parameter space and identify configurations matching with the EHT data. This can be achieved by learning the underlying relationships between physical parameters and observational constraints.

5.1 Data preparation

The datasets used in the present work are generated through CUDA-based numerical simulations. For each combination of the parameters (b, N, α) , the corresponding black hole shadow is approached and then confronted with observational data provided by EHT collaboration. This procedure is repeated under various observational constraints, resulting in distinct datasets corresponding to the $M87^*$, $Sgr A_{\text{VLTI}}^*$, and $Sgr A_{\text{Keck}}^*$ cases, each evaluated within the 1σ and 2σ confidence intervals. Based on this comparison, each sample is assigned a binary label. A value of 1 is assigned when the calculated shadow is consistent with the EHT observational limits at the given confidence level, while a value of 0 is given when it is inconsistent.

$$(b, N, \alpha) \rightarrow 1 \text{ or } 0. \quad (5.1)$$

In order to ensure the quality of the dataset, a filtering step is applied to remove non-physical or redundant configurations, retaining only parameter values within the physically allowed ranges. The features are then normalized using a standard scaling to achieve zero mean and unit variance, which improves the convergence and the stability of the training process. The dataset is subsequently divided into training, validation, and test subsets, ensuring that each black hole configuration appears in only one subset. This helps prevent data leaks and allows models to adapt effectively to unknown configurations. In fact, this process yields a clean, balanced, and well-structured dataset suitable for classification, making it possible for machine learning models to accurately determine whether a given set of parameters produces a black hole shadow consistent with the EHT observational data.

To train the machine learning models, we employ a feedforward neural NN that takes the input tuples and predicts the corresponding binary label (0 or 1). To improve accuracy and reduce sensitivity to small variations in the input parameters, we adopt a voting strategy. In this approach, for each input tuple $[M] = (b, N, \alpha)$, several equivalent representations $[M_1, M_2, \dots, M_n]$ can be generated. Each representation is processed independently by the NN. Moreover, the final prediction can be determined by a majority vote over the outputs. More precisely, the voting procedure generates several small variations of the same physical input while keeping the main physical properties unchanged. Each version has been sent independently to the FCNN model, which generates a binary prediction. The final result is then considered as the most common output among all predictions. This method provides a classification being more stable and less sensitive to small numerical changes. This can improve the reliability of the final decision. This procedure, illustrated in Fig. (9), ensures a robust classification. Moreover, it improves a generalization via different black hole configurations.

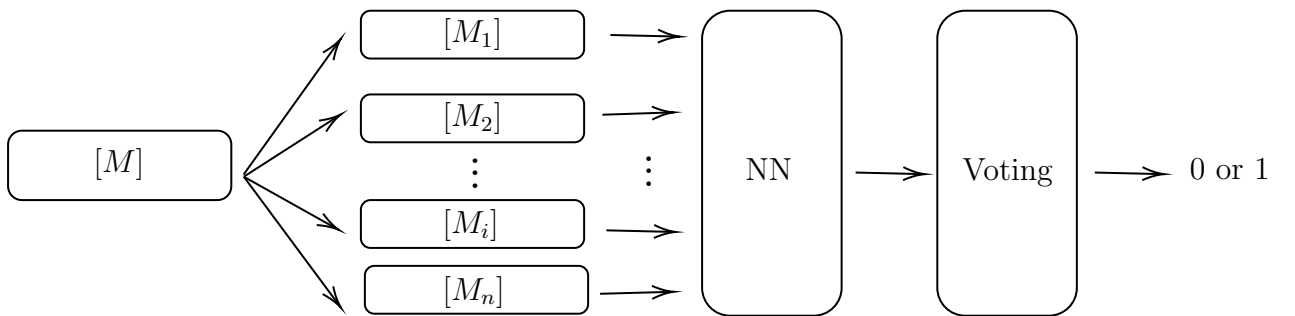


Figure 9: Voting procedure for consistency of the shadow with EHT observations

As shown in Fig. (9), each input parameter set is first processed by the neural network, which generates predictions for the corresponding configurations. These predictions are then combined using a voting scheme to produce the final output label, indicating whether the resulting black hole shadow is consistent with EHT observations. This combination of careful data preparation and an advanced learning algorithm yields a robust and accurate classification framework.

5.2 FCNN classification of NC black hole shadow consistency with EHT observations

In this part, we examine the consistency of the black hole shadow configurations with observational data from the EHT using a FCNN. The dataset consists of 20,000 samples, where each sample is characterized by the set of physical parameters (b, N, α) . To ensure a balanced dataset, we should select an equal number of samples being consistent and inconsistent with EHT observational constraints. After shuffling, the data are divided into

$$70\% \text{ training,} \quad 20\% \text{ validation,} \quad 10\% \text{ testing.}$$

To classify whether a given parameter configuration produces a black hole shadow compatible with EHT observations, we employ a FCNN model with a two-class probabilistic output. The network architecture is schemed as follows

$$N_{3 \times 2} = (F \circ G_{3 \times 32}, F \circ G_{32 \times 64}, F \circ G_{64 \times 32}, S \circ G_{32 \times 2}), \quad (5.2)$$

where $G_{n \times m}$ denotes a fully connected layer with n inputs and m outputs. F represents the ReLU activation function, and S is a softmax layer producing the final class probabilities.

The model is trained using the Adam optimizer with a binary cross-entropy loss function. We train the neural network using 2,000 data samples. During training, the learning rate is automatically adjusted to ensure the stability and the efficient convergence. Such behaviors are illustrated in Figs. (10) and (11) for $1-\sigma$ and $2-\sigma$ observational constraints, respectively.

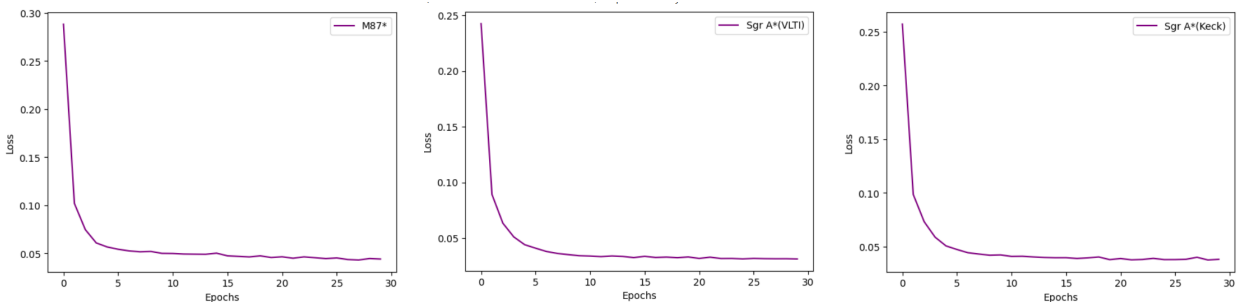


Figure 10: Training curves of the FCNN model for the $1-\sigma$ observational constraint.

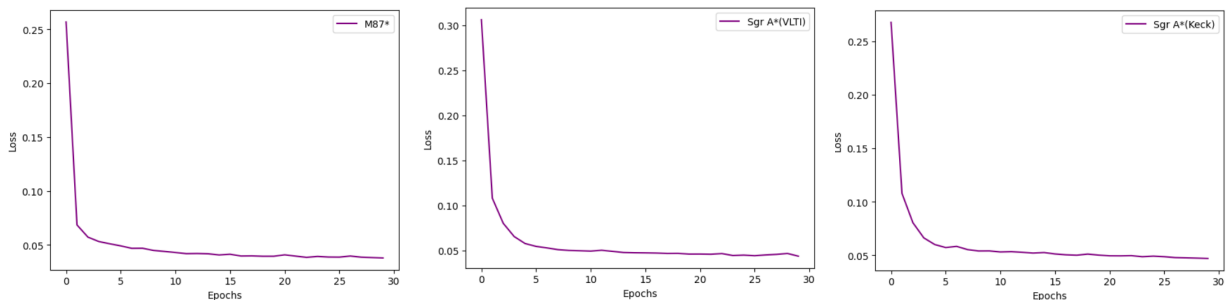


Figure 11: Training curves of the FCNN model for the $2-\sigma$ observational constraint.

As shown from these figures, the loss decreases rapidly during the initial epochs and then stabilizes. This indicates efficient learning and early convergence behaviors. The training and the validation accuracies remain consistently high across all datasets. This reveals a good generalization performance without signs of overfitting. The small fluctuations being observed in the validation loss have been expected and arise from a stochastic mini-batch optimization. However, they do not affect the global convergence behaviors. The model is further evaluated on independent test sets. Moreover, the accuracy has been computed separately for each observational case. The obtained results confirm the robustness of the classifier across all configurations. In fact, the network successfully distinguishes between configurations being compatible and incompatible with EHT observational constraints. This shows that it has learned a well-defined decision boundary in the three-dimensional parameter space coordinated by the NC black hole moduli. Roughly, the detailed performance metrics are illustrated in Tables (3) and (4) for $1 - \sigma$ and $2 - \sigma$ observational constraints, respectively.

Table 3: Model performance of the FCNN model for the $1 - \sigma$ observational constraint.

Metric	<i>M87*</i>	<i>Sgr A*_{VLTI}</i>	<i>Sgr A*_{Keck}</i>
Test Accuracy	0.978	0.9779	0.981
Voting Accuracy	0.979	0.98	0.9815

Table 4: Model performance of the FCNN model for the $2 - \sigma$ observational constraint.

Metric	<i>M87*</i>	<i>Sgr A*_{VLTI}</i>	<i>Sgr A*_{Keck}</i>
Test Accuracy	0.9804	0.9794	0.9769
Voting Accuracy	0.9815	0.9795	0.9772

To evaluate the robustness, we employ a voting system inspired by symmetry-based classification methods. For each configuration, we generate 100 perturbed samples while preserving their symmetry, and then we classify them independently. The final prediction can be obtained by majority voting, allowing to test the model stability in the face of structured perturbations. This method provides high and consistent voting accuracy across all datasets. This confirms that the classifier remains stable in the face of small deformations that preserve the symmetry. Furthermore, it generalizes the training distribution.

Although global metrics such as test accuracy and voting accuracy provide a global evaluation of the model performance, they do not offer detailed data about the distribution of classification results. To evince these issues, we approach the confusion matrices. Precisely, they are illustrated in Tables (5) and (6) for $1 - \sigma$ and $2 - \sigma$ observational constraints, respectively. Indeed, they allow a more detailed analysis of how the model assigns predictions across the two classes by explicitly showing correct classifications and misclassifications. In particular, these matrices make it possible not only to quantify the number of errors and but

also to identify any imbalance in the predictions. The results clearly reveals that the model correctly classifies nearly all samples, with only a negligible number of misclassifications. Thus, the confusion matrices provide a more complete and transparent assessment of the classifier performance beyond aggregate metrics.

Table 5: Confusion matrix using the FCNN model for the $1 - \sigma$ observational constraint.

	$M87^*$		$SgrA_{\text{VLT}}^*$		$SgrA_{\text{Keck}}^*$	
	Class 0	Class 1	Class 0	Class 1	Class 0	Class 1
Class 0	1,425	15	1,854	13	1,470	24
Class 1	27	533	24	109	16	490

Table 6: Confusion matrix using the FCNN model for the $2 - \sigma$ observational constraint.

	$M87^*$		$SgrA_{\text{VLT}}^*$		$SgrA_{\text{Keck}}^*$	
	Class 0	Class 1	Class 0	Class 1	Class 0	Class 1
Class 0	996	27	1,597	19	1,736	27
Class 1	10	967	22	362	14	223

A close examination reveals that the $1 - \sigma$ observational constraint provides slightly better and more stable performance than the $2 - \sigma$ case, particularly for the $SgrA_{\text{Keck}}^*$ dataset, where the highest accuracies are consistently obtained. Concerning the $2 - \sigma$ constraint, however, a more extensive uncertainty range has been implemented. This leads to a slight decrease in the classification performance, being noticeable in the $SgrA_{\text{Keck}}^*$ empirical findings. Thus, the model is more strictly constrained and better fitted under the $1 - \sigma$ observation regime, while remaining robust in the more flexible $2 - \sigma$ scenario.

6 Concluding remarks

In this paper, we have investigated the shadow behaviors of NC rotating and charged black holes with dark energy sectors and a cloud of strings by combining machine learning techniques, EHT observations, and CUDA-based numerical methods. First, we have analyzed the horizon structure through the metric functions of such black hole solutions, which encode the relevant shadow properties of the solutions. Then, we have applied the Hamilton–Jacobi formalism together with CUDA-accelerated simulations to determine the one-dimensional shadow curves and the energy emission rates in terms of black hole parameter variations. More specifically, we have revealed that the rotating parameter a and the charge Q affect both the size of the shadow and the energy emission rate. For large values of the parameter N and small values of α , we have found that the shadow has developed a D-like shape, showing the impact of the NC parameter b , which controls both the size and the global shape of the NC black hole shadows. After that, we have elaborated a CUDA-based numerical framework

to constrain the NC black hole parameters through a direct comparison with astrophysical observations, including those reported by the EHT collaboration. Using this framework, we have shown that the NC parameter b remains positive and below approximately 0.44 in order to be consistent with these observations. The obtained results have been then implemented within machine learning techniques to generate reliable training data for a FCNN exploited to bridge the obtained theoretical predictions with the shadow observations reported by the EHT collaboration. As a result, we have demonstrated that the fully connected and trained neural network accurately identified the shadow observations reported by the EHT collaboration. A global comparison has revealed that the $1 - \sigma$ observational constraint has yielded slightly better and more stable performance than the $2 - \sigma$ case, particularly for the $SgrA_{\text{Keck}}^*$ dataset, where the highest accuracies have been consistently obtained. Under the $2 - \sigma$ constraint, we have observed that the larger uncertainty range slightly reduced the classification performance, especially for the $SgrA_{\text{Keck}}^*$ dataset. These findings have provided the potential of CUDA-accelerated machine learning for constraining black hole parameters in non-trivial geometries including NC ones. Although the present machine learning approach supplies strong classification results, it should be interpreted in a cautious way. In future works, it would be useful to test more advanced learning methods. Moreover, it could be possible to add standard evaluation tools such as ROC curves and precision-recall analysis to better check the performance and stability of the proposed model. It would also be important to provide more details concerning the voting procedure exploited in the classification process.

This work raises several open questions for future investigations. In particular, it would be interesting to further refine the analysis of the limitations linked to the exclusive use of the shadow radius compared to EHT data, as well as to examine more closely the role of observational uncertainties and theoretical modeling assumptions in the reliability of the results.

Data availability

Data sharing is not applicable to this article.

Funding information

It is not applicable.

Acknowledgements

The author would like to thank the Department of Mathematics at the University of Aveiro and the Center for Research and Development in Mathematics and Applications (CIDMA) in Aveiro for their kind hospitality during the preparation of this work. She is very grateful to Carlos A. R. Herdeiro for his scientific support, discussions, suggestions, and encouragement. She would like to thank J. Ferreira, E. C. Filho, M. Mariano, J. Nicoules, H. Olivares, G. Ribeiro, J. J. Vázquez, and M. Wielgus for their discussions and enjoyable company. She thanks A. Belhaj for the discussions, encouragement, supervising, and collaboration on

related topics. She would also like to thank S. E. Baddis, H. Belmahi, and S. E. Ennadifi for their discussions and collaborations. The author is very grateful to the CNRST for its financial support under the PASS doctoral fellowship program.

References

- [1] M. Jemri, *Dunkl-Corrected Deformation of RN-AdS Black Hole Thermodynamics*, Theoretical and Mathematical Physics 227, 1 (2026), [arXiv:2512.19200 \[hep-th\]](#).
- [2] H. Belmahi, M. Jemri, R. Salih, *Stability and Criticality Behaviors of Accelerating Charged AdS Black Holes in Rainbow Gravity*, International Journal of Modern Physics A 40, 35 (2025), [arXiv:2507.03572 \[gr-qc\]](#).
- [3] S. E. Baddis, A. Belhaj, H. Belmahi, W. El Hadri, M. Jemri, *On RN-AdS Black Holes with a Cloud of Strings and Quintessence in Noncommutative Geometry*, [arXiv:2509.11356 \[hep-th\]](#).
- [4] T. Clifton, P. G. Ferreira, A. Padilla, C. Skordis, *Modified Gravity and Cosmology*, Phys.Rept. 513, 1 (2012), [arXiv:1106.2476 \[astro-ph.CO\]](#).
- [5] C. Herdeiro, E. Radu, E. d. S. C. Filho, N. Sanchis-Gual, *Multipolar Proca stars: electric, magnetic and hybrid solitons*, [arXiv:2605.13965 \[gr-qc\]](#).
- [6] A. Belhaj, M. Jemri, *On Thermodynamics of Charged Black Holes via Extended Space-time Derivatives*, International Journal of Modern Physics A 41, 04 (2026), [arXiv:2511.18407 \[hep-th\]](#).
- [7] P. Nicolini, A. Smailagic, E. Spallucci *Noncommutative geometry inspired Schwarzschild black hole*, Phys.Lett.B 632, 547 (2006), [arXiv:gr-qc/0510112](#).
- [8] W. El Hadri, M. Jemri, *Thermodynamics and Criticality of Noncommutative RN-AdS Black Holes*, Braz J Phys 56 23 (2026), [arXiv:2509.00926 \[hep-th\]](#).
- [9] S. E. Baddis, A. Belhaj, H. Belmahi, W. El Hadri, M. Jemri, *On RN-AdS Black Holes with a Cloud of Strings and Quintessence in Noncommutative Geometry*, [arXiv:2509.11356 \[hep-th\]](#).
- [10] M. A. A. de Paula, H. C. D. Lima, P. V. P. Cunha, C. A. R. Herdeiro, L. C. B. Crispino, *The two shadows of a single black hole: Vacuum birefringence phenomena within Einstein-Nonlinear-Electrodynamics*, [arXiv:2603.17007 \[gr-qc\]](#).
- [11] G. Bertone, *Dark matter, black holes, and gravitational waves*, Nucl.Phys.B 1003, 116487 (2024), [arXiv:2404.11513v1 \[astro-ph.CO\]](#).

- [12] A. Belhaj, H. Belmahi, M. Benali, H. El Moumni, M. Amine Essebani, M. B. Sedra, *Optical Shadows of Rotating Bardeen AdS Black Holes*, Mod.Phys.Lett.A 37, 2250032 (2022), arXiv:2202.10892 [gr-qc].
- [13] A. Belhaj, A. El Balali, W. El Hadri, H. El Moumni, M. B. Sedra, *Dark Energy Effects on Charged and Rotating Black Holes*, Eur.Phys.J.Plus 134. 9, 422 (2019), arXiv:1912.08687 [hep-th].
- [14] R. F. Rosato, S. Biswas, S. Chakraborty, P. Pani, *Excitation factors for horizonless compact objects: long-lived modes, echoes, and greybody factors*, Phys.Rev.D 113 084002 (2026), arXiv:2511.08692 [gr-qc].
- [15] R. F. Rosato, S. Biswas, S. Chakraborty, P. Pani, *Greybody factors, reflectionless scattering modes, and echoes of ultracompact horizonless objects*, Phys.Rev.D 111, 084051 (2025), arXiv:2501.16433 [gr-qc].
- [16] I. Banerjee, S. Chakraborty, S. SenGupta, *Silhouette of M87*: A new window to peek into the world of hidden dimensions*, Phys. Rev. D 101, 041301 (2020), arXiv:1909.09385 [gr-qc].
- [17] H. Belmahi, *Constrained Deflection Angle and Shadows of Rotating Black Holes in Einstein-Maxwell-scalar Theory*, International Journal of Geometric Methods in Modern Physics 23, 09, 2550248 (2026), arXiv:2411.11622 [hep-th].
- [18] A. Belhaj, M. Benali, A. El Balali, H. El Moumni and S-E. Ennadifi, *Deflection angle and shadow behaviors of quintessential black holes in arbitrary dimensions*, Class. Quantum Grav. 37 (2020) 215004, arXiv:2006.01078.
- [19] S. V. M. C. B. Xavier, P. V. P. Cunha, L. C. B. Crispino, C. A. R. Herdeiro, *Shadows of charged rotating black holes: Kerr–Newman versus Kerr–Sen*, Int. J. Mod. Phys. D 29 (2020) 2041005, arXiv:2003.14349.
- [20] A. Belhaj, M. Benali and Y. Hassouni, *Superentropic black hole shadows in arbitrary dimensions*, Eur. Phys. J. C 82 (2022) 619, arXiv:2203.06774.
- [21] A. Belhaj, H. Belmahi, A. Bouhouch, S. E. Ennadifi, M. B. Sedra, *Black holes and black strings in M-theory on Calabi–Yau threefolds with four Kähler parameters*, Eur. Phys. J. C 85, 901 (2025), arXiv:2501.07167 [hep-th].
- [22] A. Belhaj, H. Belmahi, M. Benali, W. El Hadri, H. El Moumni, E. Torrente-Lujan, *Shadows of 5D Black Holes from String Theory*, Phys. Lett. B 812, 136025 (2020), arXiv:2008.13478 [hep-th].
- [23] A. Belhaj, M. Benali, A. El Balali, W. El Hadri, H. El Moumni, E. Torrente-Lujan, *Black hole shadows in M-theory scenarios*, Int. J. Mod. Phys. D 30, 2150026 (2021), arXiv:2008.09908 [hep-th].

- [24] H. K. Sudhanshu, D. V. Singh, S. Upadhyay, Deepika, Y. Myrzakulov, and K. Myrzakulov, *Thermodynamic phase structure and shadow analysis of 4D AdS skyrmion black holes*, International Journal of Modern Physics A 41, 14, 2650089 (2026).
- [25] K. Akiyama and al., *First M87 Event Horizon Telescope Results. IV. Imaging the Central Supermassive Black Hole*, Astrophys. J. 875, L4 (2019).
- [26] K. Akiyama and al., *First M87 Event Horizon Telescope Results. V. Imaging the Central Supermassive Black Hole*, Astrophys. J. 875 L5 (2019).
- [27] K. Akiyama and al., *First M87 Event Horizon Telescope Results. VI. Imaging the Central Supermassive Black Hole*, Astrophys. J. 875 L6 (2019).
- [28] S. E. Baddis, A. Belhaj, H. Belmahi, S. E. Ennadifi, M. Jemri, *On Computational CUDA Studies of Black Hole Shadows*, arXiv:2604.14213 .
- [29] S. E. Baddis, A. Belhaj, H. Belmahi, M. Jemri, *Constraining Black Hole Shadows in Dunkl Spacetime using CUDA Numerical Computations*, Journal of High Energy Astrophysics, 51, 100541 (2026), arXiv:2510.16460 [gr-qc].
- [30] A. Elafrou, G. Thomas Collignon, *Introduction to CUDA Performance Optimization*, Nvidia.
- [31] Nvidia, *CUDA C++ Programming Guide*.
- [32] S. E. Baddis, A. Belhaj, and H. Belmahi, *CUDA Assisted Swampland and Black Hole Thermodynamics*, arXiv:2508.12378 [hep-th] .
- [33] R. Ginjupalli and G. Khanna, *High-Precision Numerical Simulations of Rotating Black Holes Accelerated by CUDA*, arXiv:1006.0663 [physics.comp-ph] .
- [34] J. v. d. Gucht, J. Davelaar, L. Hendriks, O. Porth, H. Olivares, Y. Mizuno, C. M. Fromm, H. Falcke, *Deep Horizon; a machine learning network that recovers accreting black hole parameters* Astron.Astrophys. 636, A94 (2020).
- [35] Medeiros et al., *Machine Learning Delivers Sharper Black Hole Image*, Physics 16, 63 (2023).
- [36] N. Steinle and S. Safi-Harb, *Machine learning classification of black holes in the mass–spin diagram*, Phys. Rev. D 112, 103038 (2025).
- [37] P. Nicolini, A. Smailagic, E. Spallucci, *Noncommutative geometry inspired Schwarzschild black hole*. Physics Letters B, 632 547 (2006).
- [38] M. R. Douglas, C. M. Hull, *D-branes and the noncommutative torus*, Journal of High Energy Physics, 02 008 (1998).

- [39] A. Belhaj, M. Hssaini, E. L. Sahraoui, E. H. Saidi, *Explicit Derivation of Yang-Mills Self-Dual Solutions on non-Commutative Harmonic Space*, Class.Quant.Grav. 18, 2339-2358 (2001), [arXiv:hep-th/0007137](#).
- [40] D. Berenstein, R. G. Leigh, *Non-commutative Calabi–Yau manifolds*, Phys. Review Letters, 84(20) 4737–4740 (2000).
- [41] A. Belhaj, E. H. Saidi, *On Non Commutative Calabi-Yau Hypersurfaces*, Phys.Lett. B523, 191-198 (2001), [arXiv:hep-th/0108143](#).
- [42] A. Belhaj, J. J. Manjarin, P. Resco, *On Non-Commutative Orbifolds of K3 Surfaces*, J.Math.Phys. 44, 2507-2520 (2003), [arXiv:hep-th/0207160](#).
- [43] A. Belhaj, J. Rasmussen, E. H. Saidi, A. Sebbar, *Non-commutative ADE geometries as holomorphic wave equations*, Nucl.Phys. B727, 499-512 (2005), [arXiv:hep-th/0504049](#).
- [44] P. S. Letelier, *Clouds of strings in general relativity*, Phys. Rev. D 20, 1294 (1979).
- [45] A. A. Araújo Filho, J. R. Nascimento, A. Yu. Petrov, P. J. Porfírio, A. Övgün, *Effects of non-commutative geometry on black hole properties*, Phys. Dark Univ. 46, 101630 (2024), [arXiv:2406.12015](#).
- [46] A. A. Araújo Filho, J. R. Nascimento, A. Yu. Petrov, P. J. Porfírio, A. Övgün, *Properties of an axisymmetric Lorentzian non-commutative black hole*, Phys. Dark Univ. 47, 101796 (2025), [arXiv:2411.04674](#) [gr-qc].
- [47] J. A. V. Campos, M. A. Anacleto, F. A. Brito, E. Passos, *Quasinormal modes and shadow of noncommutative black hole*, Sci. Rep. 12, 8516 (2022).
- [48] B. Hamil, B. C. Lütfüoğlu, *Phantom RN-AdS black holes in noncommutative space*, Eur. Phys. J. C 85, 313 (2025), [arXiv:2502.20514](#) [hep-th].
- [49] P. Nicolini, *Noncommutative Black Holes, The Final Appeal To Quantum Gravity: A Review*, nt.J.Mod.Phys.A 24, 1229 (2009), [arXiv:0807.1939](#) [hep-th].
- [50] F. Ahmed, A. R. P. Moreira, A. Bouzenada, *Noncommutative Geometry Inspired AdS Black Hole with a Cloud of Strings Surrounded by Quintessence-like fluid*, [arXiv:2508.00740](#).
- [51] G. Mascher, K. Destounis and K. D. Kokkotas, *Charged black holes in de Sitter space: superradiant amplification of charged scalar waves and resonant hyperradiation*, Phys. Rev. D105, 084052 (2022), [arXiv:2204.05335](#).
- [52] P. Nicolini, A. Smailagic, E. Spallucci, *Noncommutative geometry inspired Schwarzschild black hole*, Phys. Lett. B 632, 547 (2006)

- [53] A. Tiwari, R. Kaur, J. K. Bhutto, T. Vayalpurayil, M. S. Habeeb, *Criticality Quenching and Microstructure of Quintessence-AdS Black Holes*, [arXiv:2605.12632](#) [hep-th].
- [54] S. E. Baddis, A. Belhaj, H. Belmahi, M. Jemri, *Constraining Black Hole Shadows in Dunkl Spacetime using CUDA Numerical Computations*, *Journal of High Energy Astrophysics* 51, 100541 (2025), [arXiv:2510.16460](#) [gr-qc].
- [55] S. E. Baddis, A. Belhaj, and H. Belmahi, *CUDA Assisted Swampland and Black Hole Thermodynamics*, [arXiv:2508.12378](#) [hep-th].
- [56] P. Berczik, R. Spurzem, L. Wang, S. Zhong, O. Veles, I. Zinchenko, S. Huang, M. Tsai, G. Kennedy, S. Li, L. Naso, and C. Li, *Up to 700k GPU cores, Kepler, and the Ex ascale future for simulations of star clusters around black holes*, [arXiv:1312.1789](#) [astro-ph.IM].
- [57] A. G. M. Lewis, H. P. Pfeiffer, *GPU-Accelerated Simulations of Isolated Black Holes*, *Class. Quant. Grav.* 35, 095017 (2018), [arXiv:1804.09101](#) [gr-qc].
- [58] R. Ginjupalli and G. Khanna, *High-Precision Numerical Simulations of Rotating Black Holes Accelerated by CUDA*, [arXiv:1006.0663](#) [physics.comp-ph].
- [59] W. H. Press et al., *Numerical Recipes: The Art of Scientific Computing*, Cambridge University Press (2007).
- [60] J. M. Stewart, *Advanced General Relativity*, Cambridge University Press (1991).
- [61] S. Chandrasekhar, *The Mathematical Theory of Black Holes*, Oxford University Press (1983).
- [62] J. Nickolls and I. Buck, *CUDA: Scalable Parallel Programming Model for High-Performance Computing*, ACM Queue (2008).
- [63] D. B. Kirk and W. Hwu, *Programming Massively Parallel Processors: A Hands-on Approach*, Morgan Kaufmann (2016).
- [64] V. Perlick, *Ray Optics, Fermat's Principle, and Applications to General Relativity*, Springer (2000).
- [65] P. V. P. Cunha and C. A. R. Herdeiro, *Stationary Black Holes and Light Rings*, *Phys. Rev. Lett.* 124, 181101 (2020), [arXiv:2003.06445](#) [gr-qc].
- [66] C. A. R. Herdeiro, E. Radu, *Kerr black holes with scalar hair*, *Phys.Rev.Lett.* 112, 221101 (2014), [arXiv:1403.2757](#) [gr-qc].
- [67] P. V. P. Cunha, C. A. R. Herdeiro, *Shadows and strong gravitational lensing: a brief review*, *Gen.Rel.Grav.* 50, 42 (2018), [arXiv:1801.00860](#) [gr-qc].

- [68] P. V. P. Cunha, C. A. R. Herdeiro, B. Kleihaus, J. Kunz, E. Radu, *Shadows of Einstein-dilaton-Gauss-Bonnet black holes*, Phys. Lett. B 768, 373 (2017), [arXiv:1701.00079 \[gr-qc\]](#).
- [69] C. A. R. Herdeiro, E. Radu, *Asymptotically flat black holes with scalar hair: a review*, Int. J. Mod. Phys. D 24, 1542014 (2015), [arXiv:1504.08209 \[gr-qc\]](#).
- [70] S. W. Wei, Y. C. Zou, Y. X. Liu, R. B. Mann, *Curvature radius and Kerr black hole shadow*, JCAP 08, 030 (2019), [arXiv:1904.07710](#).
- [71] A. Elafrou, G. Thomas Collignon, *Introduction to CUDA Performance Optimization*, Nvidia.
- [72] Nvidia, *CUDA C++ Programming Guide*.
- [73] Y. Décanini, A. Folacci, G. Esposito-Farèse, *Universality of high-energy absorption cross sections for black holes*, Phys. Rev. D 83, 044032 (2011), [arXiv:1101.0781 \[gr-qc\]](#).
- [74] S.-W. Wei, Y.-X. Liu, *Relationship between high-energy absorption cross section and strong gravitational lensing for a static and spherically symmetric black hole*, Phys. Rev. D 84, 041501 (2011), [arXiv:1103.3822 \[hep-th\]](#).
- [75] V. Perlick, *Calculating black hole shadows: Review of analytical studies*, Phys. Rep. 924, 1 (2022), [arXiv:2105.07101 \[gr-qc\]](#).
- [76] P. Kocherlakota et al. [Event Horizon Telescope], *Constraints on black-hole charges with the 2017 EHT observations of M87**, Phys. Rev. D 103, 10, 104047 (2021).
- [77] L. Chakhchi, H. El Moumni and K. Masmar, *Signatures of the accelerating black holes with a cosmological constant from the Sgr A* and M87* shadow prospects*, Phys. Dark Univ. 44, 101501 (2024).
- [78] D. J. Gogoi and S. Ponglertsakul, *Constraints on quasinormal modes from black hole shadows in regular non-minimal Einstein Yang Mills gravity*, Eur. Phys. J. C 84, 6652 (2024).
- [79] N. Steinle, S. Safi-Harb, *Machine learning classification of black holes in the mass-spin diagram*, Phys. Rev. D 112, 10, 103038 (2025), [arXiv:2508.14316](#).
- [80] J. W. Lee, Z. Y. Kim, *Black hole/quantum machine learning correspondence*, [arXiv:2506.09678](#).
- [81] W. Cui, X. Gao, M. Karkheiran, J. Wang, *Machine Learning Free Quotients of CICYs*, [arXiv:2508.19157 \[hep-th\]](#).
- [82] L. F. S. Scabini, O. M. Bruno, *Structure and Performance of Fully Connected Neural Networks: Emerging Complex Network Properties*, [arXiv:2107.14062](#).

- [83] J. Carifio, J. Halverson, D. Krioukov, B. D. Nelson, *Machine Learning in the String Landscape*, JHEP 09, 157 (2017), [arXiv:1707.00655 \[hep-th\]](#).
- [84] Y.-H. He, *Deep-Learning the Landscape*, Phys. Lett. B 774, 564 (2017), [arXiv:1706.02714 \[hep-th\]](#).